LASER INTERFEROMETER GRAVITATIONAL WAVE OBSERVATORY
- LIGO -
CALIFORNIA INSTITUTE OF TECHNOLOGY
MASSACHUSETTS INSTITUTE OF TECHNOLOGY

Technical Note	LIGO-T1400509-v1	2014/08/22

Optimization of Michelson Interferometer Signals in Crackle Noise Detection

Horng Sheng Chia, Gabriele Vajente

Distribution of this document:

LIGO Scientific Collaboration

California Institute of Technology
LIGO Project, MS 18-34
Pasadena, CA 91125
Phone (626) 395-2129
Fax (626) 304-9834
E-mail: info@ligo.caltech.edu

Massachusetts Institute of Technology
LIGO Project, Room NW17-161
Cambridge, MA 02139
Phone (617) 253-4824
Fax (617) 253-7014
E-mail: info@ligo.mit.edu

LIGO Hanford Observatory
Route 10, Mile Marker 2
Richland, WA 99352
Phone (509) 372-8106
Fax (509) 372-8137
E-mail: info@ligo.caltech.edu

LIGO Livingston Observatory
19100 LIGO Lane
Livingston, LA 70754
Phone (225) 686-3100
Fax (225) 686-7189
E-mail: info@ligo.caltech.edu

http://www.ligo.caltech.edu/

Abstract

The search for crackle noise [1] [2] has been limited by the presence of various sources of noise, including laser frequency noise, laser intensity noise and the misalignment of end mirrors in the Michelson interferometer. We developed an optimization algorithm that finds the best parameters that minimize the coupling of these noises into the output. These parameters include microscopic and macroscopic length difference of Michelson arms, and the angular alignment of end mirrors.

1 Motivation

Noise reduction is one of the most crucial parts in LIGO science. It has long been suspected that mechanical crackling noise generated in Advanced LIGO suspension components and joint interfaces contributes to the noise spectrum. By crackle noise, we mean the impulsive release of energy, acoustic emissions, or changes in geometry of attachments between suspension elements, or the stress fields in the element themselves [1].

The crackle experiment [1][2] is set up to measure crackle noise at the displacement sensitivity of Advanced LIGO. Although Advanced LIGO has an observational band of 10Hz-10kHz, we are interested to measure crackle noise at 10Hz, the low frequency regime, with a sensitivity of $10^{-15}\mathrm{m}/\sqrt{Hz}$. Two reasons follow: (i) the crackle noise is partially filtered by suspension systems [2], which have resonant frequencies of a few Hz, so only noise at lower frequencies are of interest; (ii) crackle noise is expected to decrease with frequency, approximately like $1/f$.

A Michelson interferometer is one of the most precise techniques to measure relative distance changes [3]. Since crackle noise is incoherent in nature, we can use the Michelson interferometer setup to measure differential displacements of maraging steel blade suspensions at the end of both interferometer arms [2].

Our detection sensitivity of crackle noise is fundamentally limited by various sources of noise, including laser frequency noise, laser intensity noise and end mirror misalignments. Fortunately, these noise couple minimally into our output readings if we adjust the parameters of the experimental setup suitably. In the past, the ideal parameters could only be determined using trial and error. In addition, these parameters constantly drifted away from the ideal adjustment due to random environmental influences, and had to be readjusted very frequently. Hence, measurements can be tedious and laborious. The goal of this project is to develop an algorithm that adjusts these parameters automatically and accurately to facilitate measuring efforts in the upgraded setup.

2 Michelson Interferometer

In the crackle experiment, the parameters that we adjust are the arm lengths of Michelson interferometer and the end mirror angular alignments. Since the only relevant distance in the Michelson interferometer is the relative distance between two arms, we fix the length of one arm, and translate the other arm using a piezomotor driven translation stage. The end mirror alignments are controlled using magnetic actuators, two on each mirror to control all four degrees of freedom [2]

The output signal of Michelson interferometer is taken as the difference between signals read at the symmetric and antisymmetric ports. The reason of this approach will be evident as we discuss laser intensity noise in section 4.

The optimization algorithms developed are first being tested in simulation before being implemented in the real crackle experiment. The simulations are done with the MIST open source toolbox [4] in a MATLAB environment. The Michelson interferometer configuration file is attached in appendix [1], based on figure 1.

Since measurement uncertainties are present in the real crackle experiment, we have created two functions for adding them in the simulation. One introduces uncertainties with a given absolute value range, another introduces noise based on percentage uncertainty of the measurement. (See appendices [2] and [3]). Both functions assume that the uncertainty is given by a uniform distribution. The magnitude and type of measurement uncertainty (either one of the two functions above) used will be dependent on our past experiences of the crackle experiments. The values used in the simulation are added in all of the codes in the appendix.

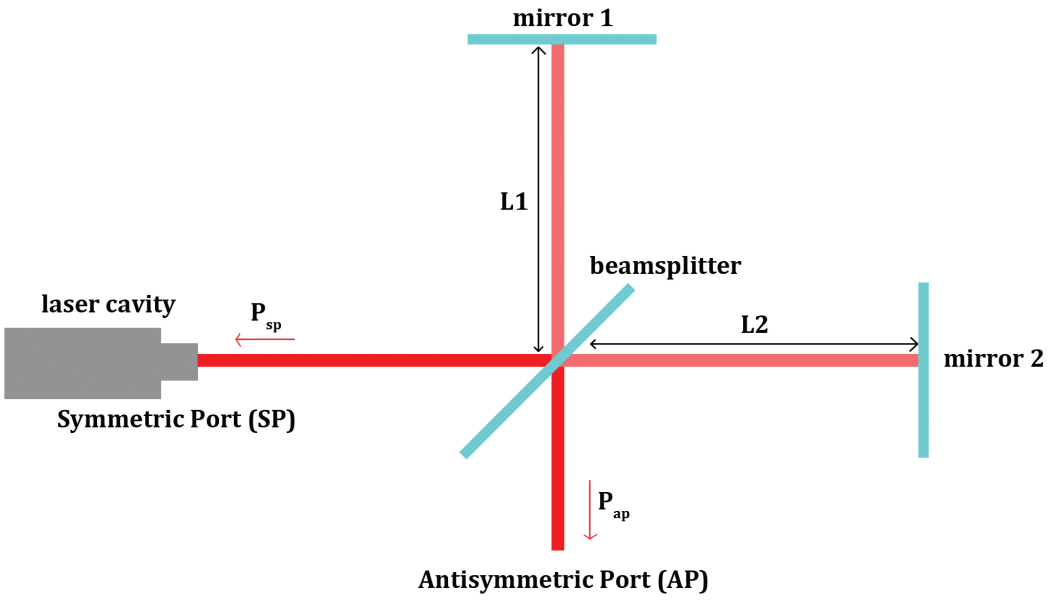

Figure 1: Optical configuration of Michelson interferometer simulation.

3 Laser Frequency Noise

Laser frequency noise is the fluctuation of frequency of laser with time. This arises from various sources inherent in the optical system, and are usually very difficult to be eliminated. These sources include noise generated by NPRO crystal oscillator, changes in laser cavity length, temperature, pumping power and so on. However, the amount of laser frequency noise coupled into the output ports, namely the optical gain of laser frequency noise, is proportional to the macroscopic length difference between the two arms, expressed by the relationship below: [2]

$$g_{\text{freq}} = \Delta L/\nu \tag{1}$$

where g_{freq} is the optical gain of laser frequency noise (units m/Hz), ΔL is the macroscopic length difference between both arms and ν is the frequency of laser. Hence, our aim is to adjust the macroscopic length difference of both arms, to minimize coupling of laser frequency noise into our output signal.

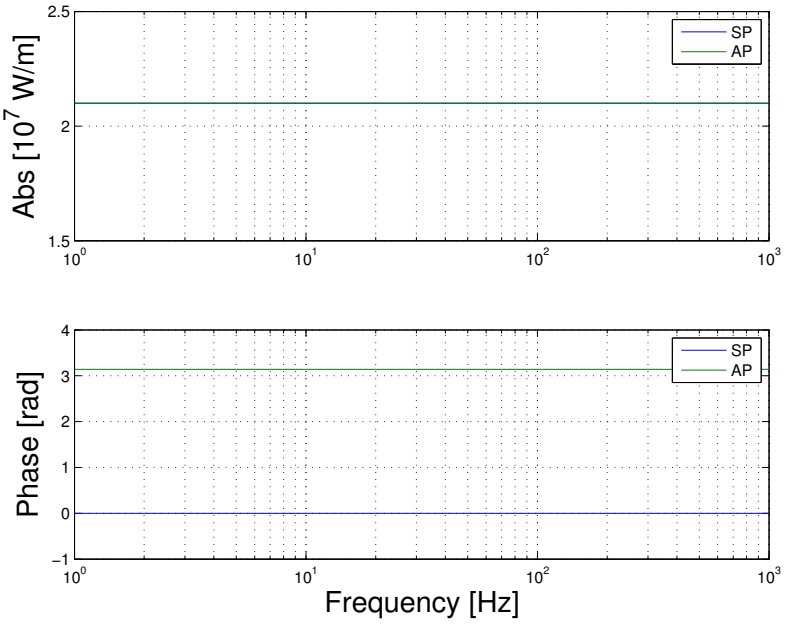

Figure 2: Transfer function of symmetric(SP) and antisymmetric (AP) ports from longitudinal motion of mirrors to the photodiode signals. Top subplot shows the ratios of output power against input power with respect to the frequency of oscillation of mirrors at both ports, TF_{mich}, which are shown to have same absolute value. The bottom subplot is the phase at both ports with respect to the frequency of oscillation of mirrors, with ports at 0 and π respectively. This explains the antisymmetric fringe pattern in Figure 8.

To simulate equation 1, we need to represent laser frequency noise in terms of the equivalent amount of noise coupled due to arm length difference. We compute two transfer functions: one from the longitudinal motion of mirrors to power measured at photodiodes, TF_{mich} as shown in Figure 2, and another from the laser frequency to power measured at photodiodes, TF_{las} as shown in Figure 3. The laser frequency noise coupling is then obtained by $g_{freq} = TF_{mich}/TF_{las}$. See appendices [4, 5].

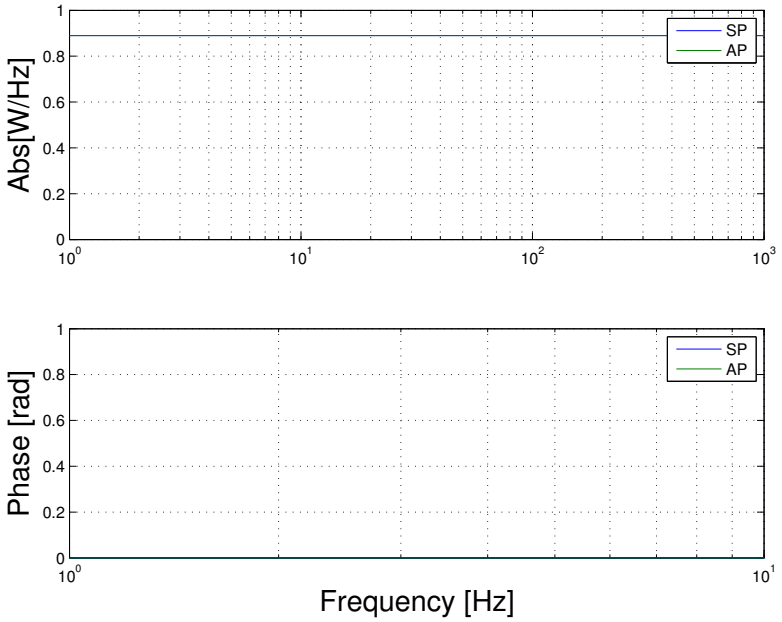

Figure 3: Transfer functions of symmetric (SP) and antisymmetric (AP) ports from laser frequency modulation to the photodiode powers, when the macroscopic length difference of the two arms is zero. Top subplot shows the ratios of output power against input power with respect to modulation frequency, TF_{las}. The bottom subplot is the phase at both ports with respect to the laser frequency modulation. Notice that the SP and AP values are the same, as we expected from equation 1.

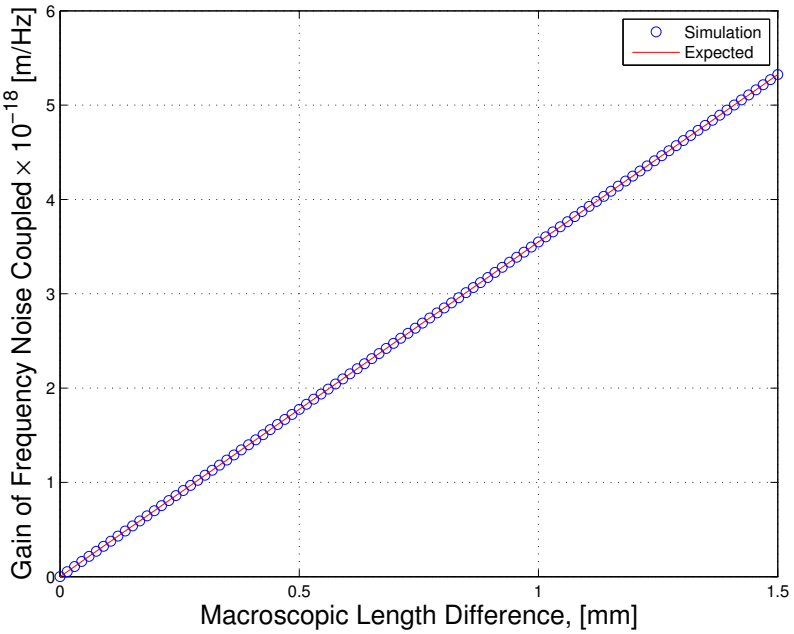

Figure 4: Optical gain of laser frequency noise vs macroscopic length difference of both arms. Simulation is in good agreement with equation 1.

In a more realistic model, measurement uncertainties in the transfer function and macroscopic length of the movable arm should be taken into account. Given the linear relationship in equation 1, we minimize laser frequency coupling using the following method (see appendix [6]):

1. Sample two points: one at the current position of the movable arm, and another at 1 mm shorter than the current length. This is about 1/10 of the travel range of the piezomotor driven translation stage.
2. Calculate the gradient between two points, use linear extrapolation to estimate the position that corresponds to zero g_{freq}.
3. Move the arm to the estimated position.
4. Repeat steps 1 to 3 until the laser frequency noise gain hits a value below the threshold.

In the real crackle experiment, the length of stationary arm is 316 mm. The piezomotor driven translation stage that controls the length of the movable arm [2] has a travel range of 12 mm, and the minimum step size is 0.05 μm. Figure 5 shows the case when initial length of movable arm is set at 328 mm. This value correspond to (316+12) mm, which is an extremum of the allowed range of movable arm length. We also simulate the interferometer using a laser frequency gain threshold value $g_{\text{freq}} < 0.1 \times 10^{-17}$ m/$\sqrt{Hz}$, with 1% measurement uncertainty in the transfer function. The algorithm described above is repeated 100 times and the statistical data is collected.

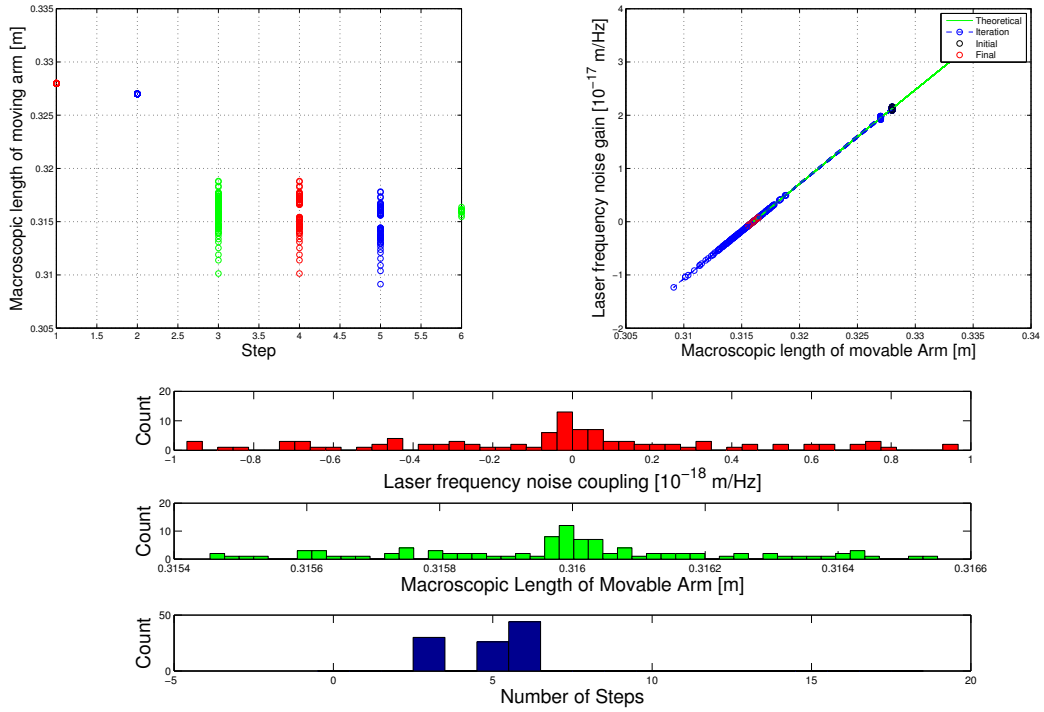

Figure 5: 100 repeated measurements of the initial length of movable arm at 328 mm.

Figure 5 shows that the algorithm performs extremely well. Left graph of top row shows the timeline of the change of macroscopic length of movable arm. Notice that each iteration usually comes in a group of 3 points (see step 1-2 in algorithm above): red is first sampled point, blue is the second sampled point, and green is the extrapolated point. The y-values of the first red and the first

blue points remain approximately unchanged because they correspond to the initial position and a step away from initial position respectively. These points are used to estimate the extrapolated point, which correspond to the range of green points in step 3. If the threshold value is not met, the iteration is repeated. Right graph of top row shows the iteration process of g_{freq} against length of movable arm. Notice that the black points concentrate about the initial position, and the red points concentrate about the length of stationary arm, as expected. Bottom row shows the statistics of the 100 repeated measurements. Notice that the laser frequency noise coupling and macroscopic length of movable arm peak about 0 m/Hz and 316mm respectively, as expected. The algorithm also takes a range of 4-6 sample points to complete the algorithm, which is efficient.

A natural question follows: how large does the percentage uncertainty of measured transfer function has to be for the algorithm to fail? Figure 6 shows that at a measurement percentage uncertainty of approximately 5%, the algorithm starts to have occasional iterations that deviate greatly from the regime close to the length of immovable arm. Some of the lengths are also beyond the range of translation stage. Hence, we can crudely say that the algorithm works well only when the transfer function percentage uncertainty is below 5%.

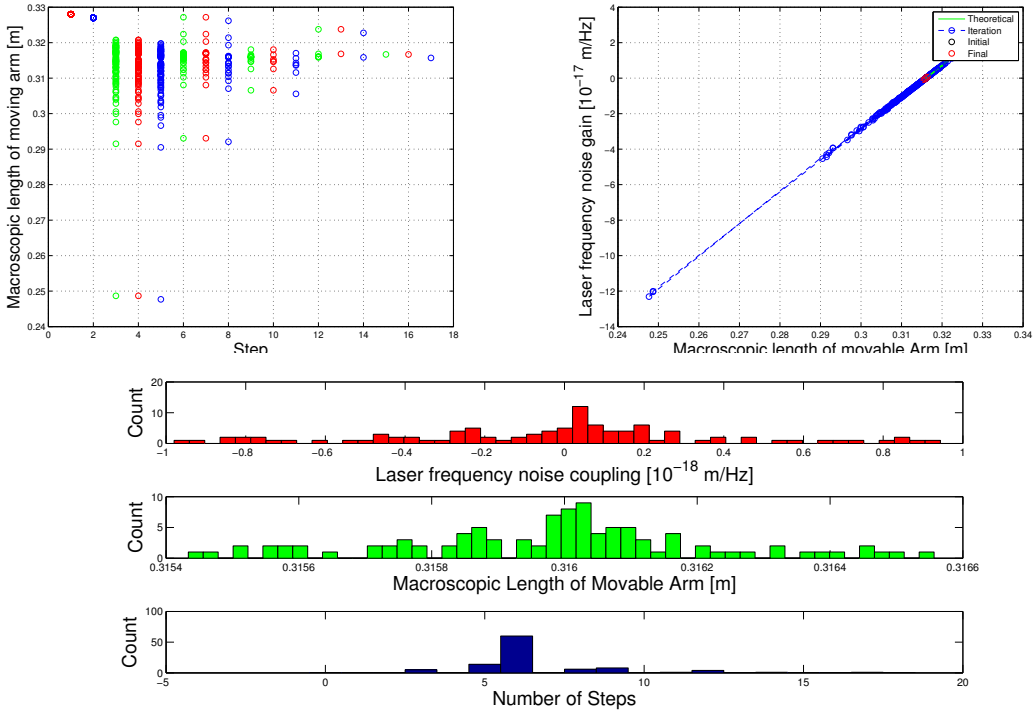

Figure 6: Implementations of the algorithm, with transfer function percentage uncertainty of 5%

4 Laser Intensity Noise

4.1 Locking

Laser intensity noise is the fluctuation of laser output power, and couples to the ports proportionally to the power incident on the photodiode, given by the relationship below [2]:

$$g_{\mathrm{RIN}} = \frac{P_{\mathrm{AP}}}{P_{\mathrm{i}}} = sin^2\phi + C_{\mathrm{D}} \tag{2}$$

where g_{RIN} is the optical gain of laser intensity noise, P_{AP} is the power incident at antisymmetric port, P_i is the initial power of laser, ϕ is the Michelson fringe tuning, and C_D is the fringe contrast defect, which arises mainly due to different reflectivities of mirrors on both arms and misalignment of optical elements.

Another common way of representing laser intensity noise is by the relative intensity noise (RIN) factor, defined as

$$RIN = \frac{\delta P}{P} \tag{3}$$

where δP is the amplitude of laser power fluctuation, and P is the mean laser power.

Laser intensity noise is eliminated if we take the difference between symmetric and antisymmetic port signals as the output signal. In an ideal case where no asymmetries in the interferometer are taken into account, this happens if we operate the interferometer at the half fringe point, where the phase difference $\Delta\phi$ between both arms satisfy the relationship

$$\Delta\phi = \frac{n\pi}{2} + \frac{\pi}{4} \tag{4}$$

where n is any integer. The half fringe condition is also the point where we obtain maximum sensitivity to differential displacement, because it corresponds to the point with steepest gradient of the fringe pattern (see figure 8). To achieve this, a negative feedback mechanism called locking is implemented, which allows the Michelson interferometer to operate at the point where both symmetric and antisymmetric ports have equal power.

Notice that as long as the Michelson interferometer is locked, laser intensity noise does not couple into the output. From equation 2 and 3, laser intensity noise is proportional to the power of laser incident at the ports. Since locking is by virtue the mechanism that allows interferometer to operate at the point where the power readouts at both ports are equal, by taking the difference between port signals, laser intensity noise cancels out each other. Hence, it is worth emphasizing that the only crucial factor to eliminate laser intensity noise is to ensure that interferometer arms are locked. The algorithm for locking is readily available in the MIST optical toolbox. Figure 7 shows a simulation example of the timeline of locking.

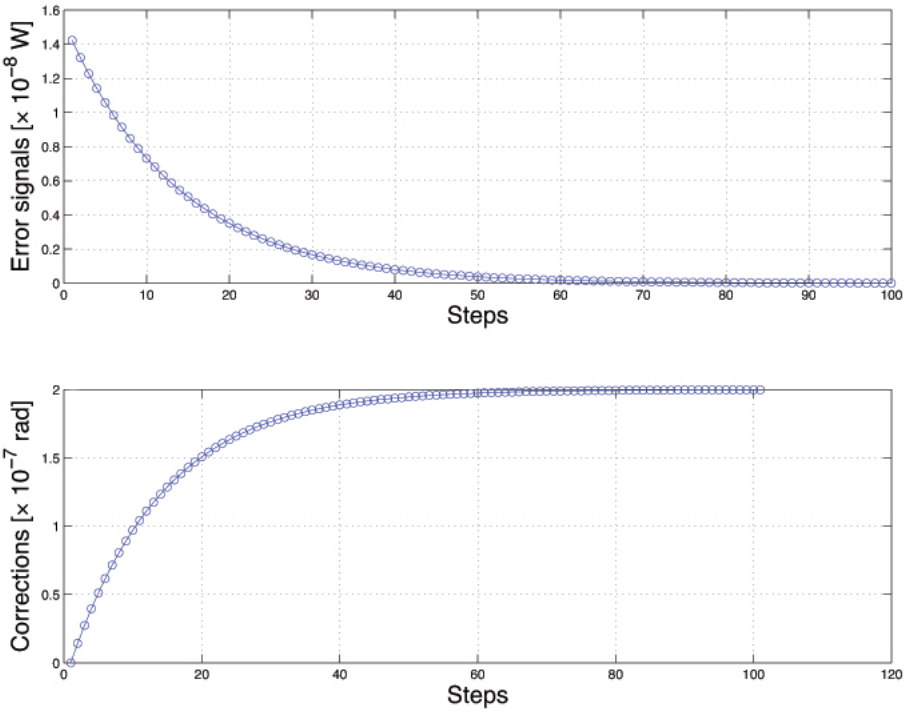

Figure 7: Locking feedback mechanism after a microscopic perturbation of 2×10^{-7} rad is introduced in one arm. Top subplot shows the error signal between powers incident at both ports. Bottom subplot shows the correction on microscopic length difference between both arms to achieve locking.

4.2 Adjusting relative gain

Inherent asymmetries in the system, such as different mirror reflectivities and photodiode gains, prevent us from having the same fringe pattern amplitudes at both ports. This reduces our sensitivity to differential displacement. Notice from first column of Figure 8, the intersection points between symmetric and antisymmetric patterns do not correspond to maximum gradient. Maximum sensitivity is achieved only when we equalize the power readouts, leading the operating point to the half fringe point. This can be done by carefully tuning the relative gains of both ports. The relative gain can only be determined empirically, hence it is vital that we scan through the fringe pattern to obtain the average power across the fringe pattern at the ports.

Here our assumption is that noise is perfectly random and hence averages to zero. Two simulation examples are shown in Figure 8. The following steps describe the basics of our strategy (see appendix [7]).

1. Scan through fringe pattern at both ports.
2. Calculate the average powers incident at both symmetric and antisymmetric ports across the fringe patterns.
3. Calculate the ratio of the average value of powers calculated at step 2.
4. Increase gain of the port that receives lower power and equalize the power of both ports.
5. Lock the Michelson interferometer to the appropriate microscopic tuning. This operating point should be at half fringe point now.

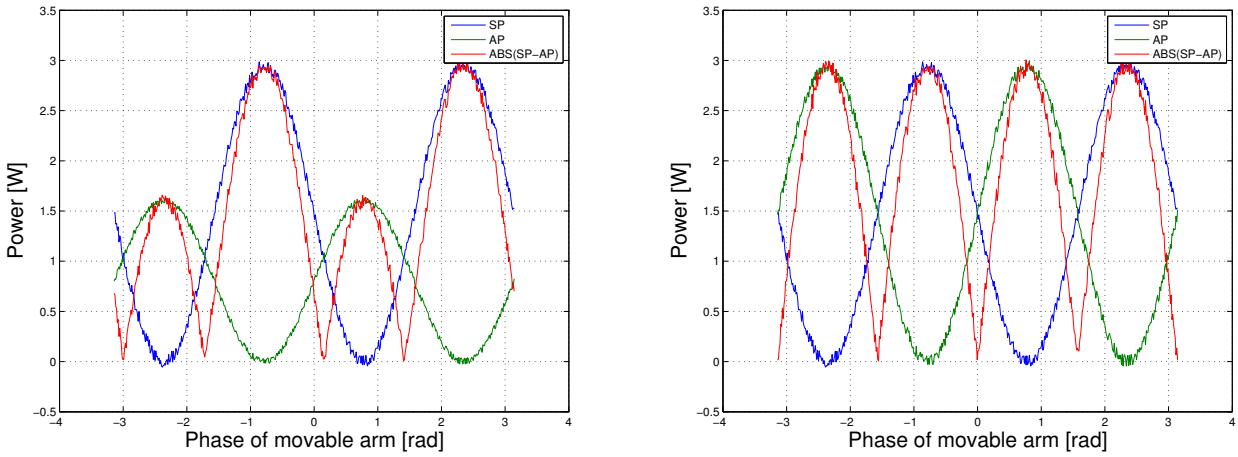

(a) Before: g_R = 1.84; after: g_R =0.86.

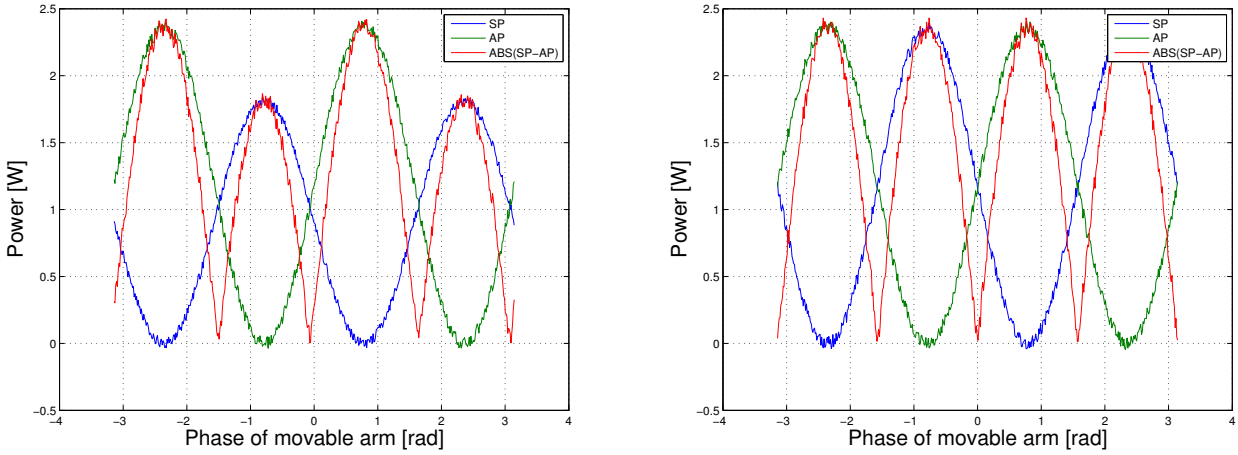

(b) Before: g_R = 0.77; after g_R = 1.04.

Figure 8: Suppose we define relative gain, $g_R = \frac{P_{SP}}{P_{AP}}$. First column shows fringe pattern before relative gain adjustment. Second column shows that after relative gain adjustment.

Figure 8 shows that the algorithm works well. Notice that before adjusting the relative gain, the AP and SP graphs do not intersect at x-axis=0 (see left column), but they do after the adjustment (see right column). This means that before relative gain adjustment, the locking is not at its optimal point. After the adjustment, half-fringe point is achieved, hence both fringe patterns are equal, except with a phase shift of π.

5 Mirror Misalignment

5.1 Laser Beam

We include a brief discussion of theory of laser beam in this subsection, which provides the reader crucial insight into fixing the misalignment of mirrors. Laser beams behave similarly as planar waves, except their transverse intensity distribution varies with distance from the centre, and additional parameters such as beam radius and radius of curvature at each transverse plane should be taken into account. From the wave equation, by separation of variable, and consider only the spatial component (assuming steady state), Helmholtz equation is obtained using paraxial approximation [5, 6].

$$\nabla^2\psi + k^2\psi = 0 \tag{5}$$

where ψ is the wavefunction of the laser beam. We define z to be the direction of propagation, and the x-y plane the transverse plane. The fundamental mode of the equation above has the following expression:

$$\psi_o = \sqrt{\frac{2}{\pi w^2}} e^{i(kz + \frac{k(x^2+y^2)}{2R} + \Phi)} e^{-\frac{x^2+y^2}{w^2}} \tag{6}$$

where k is the wavenumber, R the radius of curvature of the wavefront and w the beam radius at z. The first term on right hand side is just a normalisation constant, the second term illustrates the phase change as we move along the x, y, and z directions, Φ is just an arbitrary phase, while the last exponential illustrates the Gaussian intensity profile. The fundamental mode is hence a Gaussian beam. Higher order mode solutions that satisfy equation 5 can also be found, and they form a complete set of linearly independent solution for a laser beam. These solutions are called Gauss-Hermite modes (for rectangular symmetry) and Gauss-Laguerre modes (for circular symmetry) [5, 6]. These higher order modes are represented by $\Psi_{m\,n}$, where n and m are the integers that describe the order of the modes. This will be useful for our discussion later.

Further expressions of R and w as functions of the propagation distance z can be derived from equation 5, given by [5, 6]

$$w^2(z) = {w_o}^2 \left[1 + (\frac{\lambda z}{\pi {w_o}^2})^2\right] \tag{7}$$

$$R(z) = z\left[1 + (\frac{\pi {w_o}^2}{\lambda z})^2\right] \tag{8}$$

where w_o is the beam waist size, λ the wavelength of laser, and the other expressions have their usual meaning. These expressions imply that at z=0, laser beam has minimum beam radius and the wavefront is planar.

From equation 7, the beam radius varies with z, with the shape of a hyperbola, as shown in Figure 9. The divergence angle θ is defined as the angle between an asymptote and the optical axis, given by [5, 6]

$$\theta = \frac{\lambda}{\pi w_o} \tag{9}$$

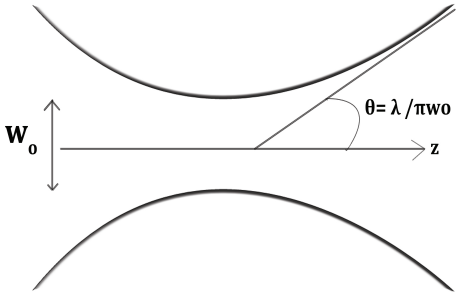

Figure 9: Beam profile.

5.2 Fringe Contrast

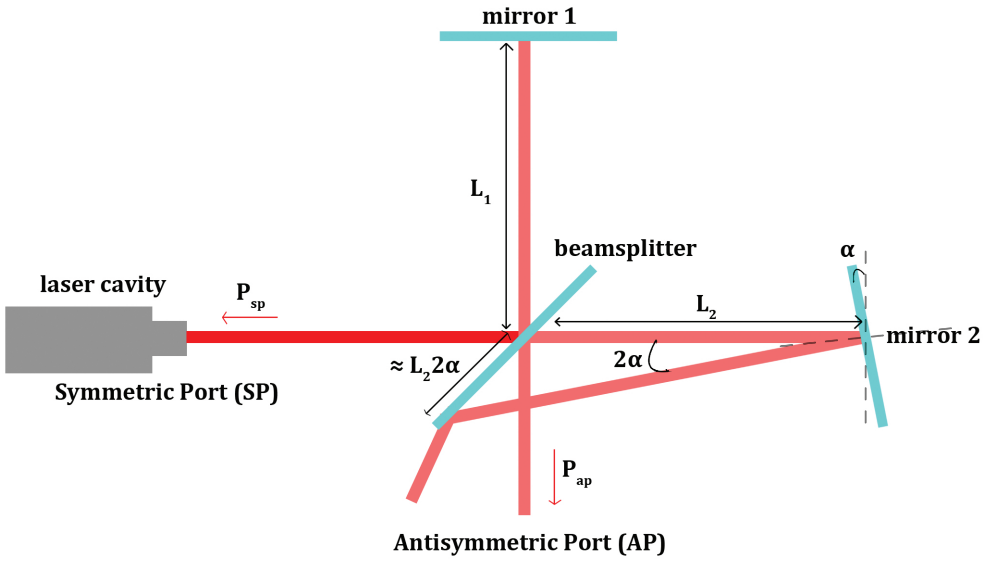

Figure 10: Configuration of optical simulation with a tilted mirror. Note the exaggerated misalignment angle.

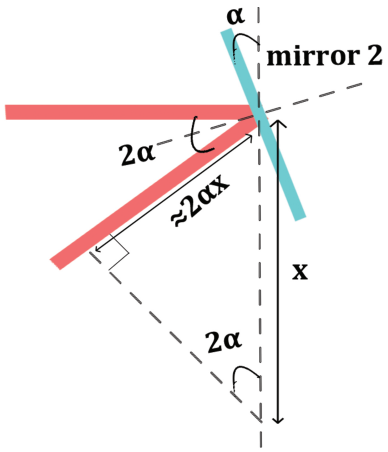

Figure 11: Diagram of the effect of mirror misalignment on phase addition on laser beam. Note the exaggerated misalignment angle. Small angle approximation is used.

The crackle experiment will be set up such that when both arm lengths are equalized, the radii of curvature of laser beams at the end mirrors are infinite, i.e. wavefronts are planar and the beam waist is w_o = 300 μm. This can be done by a series of optical elements, such as converging and diverging lenses, added into the setup. From our previous discussion, this means that we can set z=0 at both end mirrors.

Without loss of generality, let us consider the simplest case where only one mirror is tilted by an angle α, as shown in Figure 10. Using small angle approximation, the centre of a Gaussian beam that is reflected by the tilted mirror will be shifted by a distance $2L_2\alpha$ away from the centre of the other beam, where L_2 is the length of Michelson arm with tilted end mirror. Hence the wavefunction will be given by this form:

$$\psi_r = \sqrt{\frac{2}{\pi w^2}} e^{i(kz + \frac{k[(x-2L_2\alpha)^2+y^2]}{2R} + \Phi + 2k\alpha x)} e^{-\frac{(x-2L_2\alpha)^2+y^2}{w^2}} \tag{10}$$

Notice that equation 10 above differs from equation 6 by two features: first, the centre of equation 10 Gaussian is shifted along the x-direction; second, an additional phase term of $2ik\alpha x$ arises due to reflection at the tilted mirror, as explained by Figure 11. We present here a simple derivation of the relationship between scalar product of two wavefunctions and the fringe contrast of the pattern detected at the photodiodes. Let ψ_1 and ψ_2 be two general wavefunctions that superpose with one another at the same spatial point (in the Michelson interferometer, this occurs at the beamsplitter), the power P incident at either photodiode is

$$\begin{aligned} P &= \int\int |\psi_1 + \psi_2|^2 dxdy \\ &= \int\int \{|\psi_1|^2 + |\psi_2|^2 + 2Re[\psi_1 {\psi_2}^*]\} dxdy \\ &= 2\{1 + \int\int Re[\psi_1 {\psi_2}^*] dxdy\} \end{aligned} \tag{11}$$

where we used wavefunction normalization in the third line. The first term in curly brace on the third line is the average power incident at photodiodes, while the second integral term is the sinusoidal interference pattern. We can therefore deduce that

$$\begin{aligned} P_{max} &= 2\{1 + \int\int Re[\psi_1 {\psi_2}^*] dxdy\} \\ P_{min} &= 2\{1 - \int\int Re[\psi_1 {\psi_2}^*] dxdy\} \\ \Longrightarrow \int\int Re[\psi_1 {\psi_2}^*] dxdy &= \frac{P_{max} - P_{min}}{P_{max} + P_{min}} \end{aligned} \tag{12}$$

Hence, using equations 6, 10 and 11, the scalar product of two wavefunctions at the beamsplitter is given by

$$\int\int Re[\psi_r {\psi_o}^*] dxdy = e^{-\frac{2{L_2}^2\alpha^2}{w^2} - \frac{k^2 w^2 \alpha^2}{2} + \frac{k^2 w^2 L_2 \alpha^2}{R} - \frac{k^2 {L_2}^2 w^2 \alpha^2}{2R^2}} \tag{13}$$

where the first two terms in equation 13 arise due to the shifted Gaussian centre as depicted in figure 10, and the remaining terms due to the difference in curvature of split beams wavefronts when they are incident at the beamsplitter.

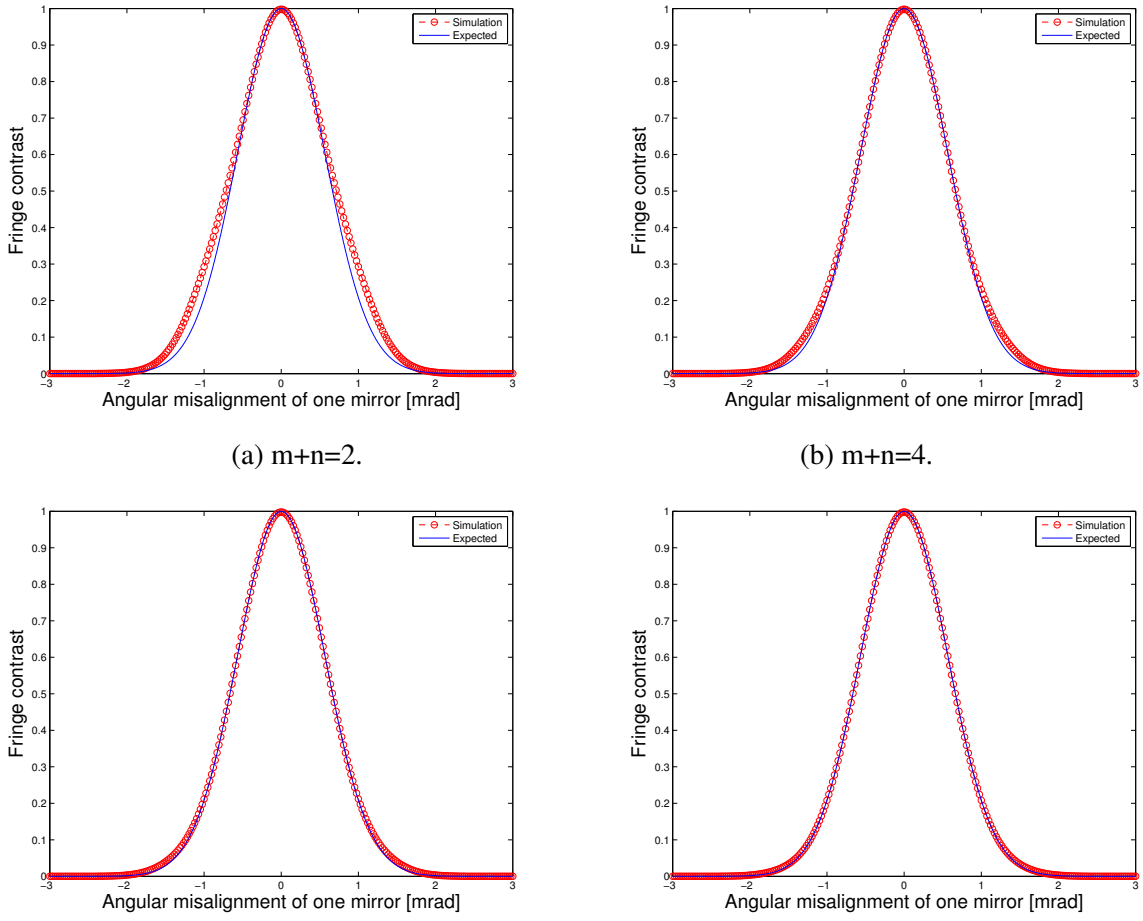

(a) m+n=2.

(b) m+n=4.

(c) m+n=6.

(d) m+n=8.

Figure 12: Fringe contrast against mirror angular misalignment.

Figure 12 shows the graph based on equation 13 and the MIST simulation with varying number of modes. (See appendix [8]) It is observed that for n+m $\geq$ 6, the simulation is in good agreement with the model. In principle we can increase the value n+m to as large as we want to get the most accurate waveform, but that will take enormous amount of computational time and will be impractical. We decided that n+m=6 is a good balance between computational time and accuracy.

5.3 Tackling misalignment (gradual step method)

Our aim is to adjust the mirror alignment so that maximum fringe contrast is observed. Since each mirror can rotate about x- and y-axes, there is a total of four degrees of freedom involved. However, since what really matters is the relative alignment between the mirrors, we can in principle adjust only two orthogonal degrees of freedom, i.e. one about x-axis and another about y-axis.

Using our prior information of figure 12, and given a certain misalignment of unknown value α, we adopt the following method (see appendix [10]:

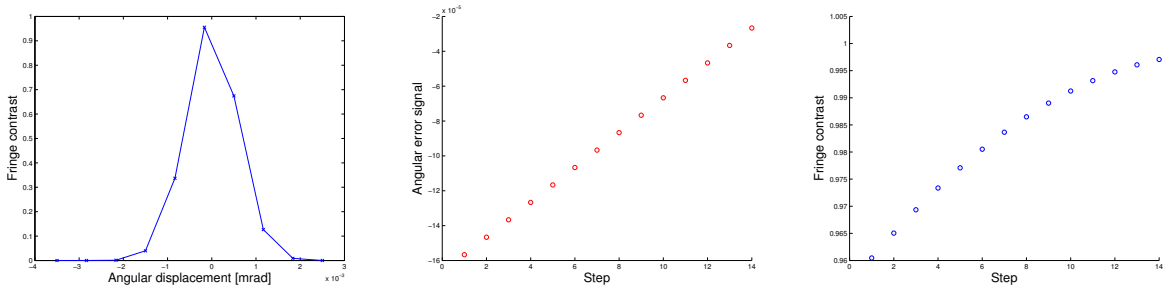

(a) α =-0.0005rad

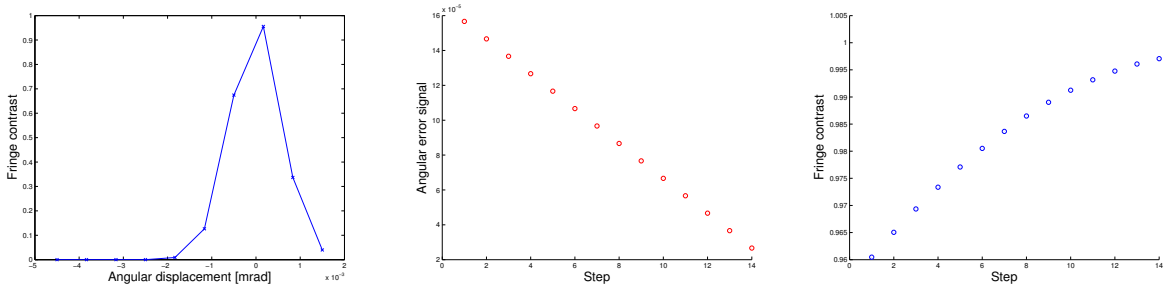

(b) α = -0.0015rad

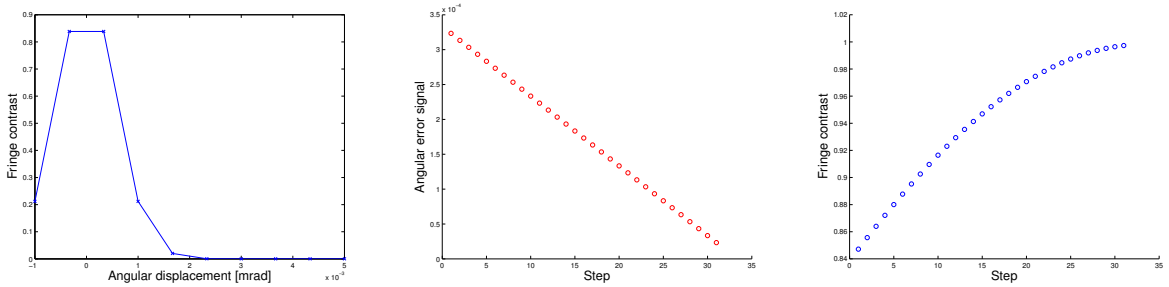

(c) α = 0.002rad

Figure 13: Simulation results for three different initial misalignment at one end mirror. Each example is given in a row. The first column is the fringe contrast pattern sampled at 10 equally spaced points, as described in step 2. The second column shows the increase or decrease in angular displacement with increasing step, described in step 4. The third column is the change in fringe contrast measured with increasing step, described in step 5.

1. Sample a few, say 10, equally spaced points across the range (α-0.003, α+0.003) radians. This is the 5-sigma range of angular misalignment obtained from Figure 12. The results are shown in first column of Figure 13.
2. Align the mirror to the sampled point with maximum value of fringe contrast.
3. Choose a step size of angular displacement. This value should be limited by the sensitivity of angular control, but should also be small enough such that fringe contrast changes incrementally. From Figure 12, a suitable step size is 10μrad.
4. Take a step of 10μrad at a random direction. If the fringe contrast increases, repeat step 3. If the fringe contrast decreases, reverse the step at another direction. Results shown in second column of Figure 13.
5. Repeat step 3 until the mirror aligns at the position such that it achieves maximum fringe

contrast. Shown in third column of Figure 13.
6. Repeat steps 1 to 5 for the other degree of freedom.

This first approach poses various problems. Firstly, the step size is fixed, which may lead to the possibility of infinite oscillation of the iteration if the step size is too large, or an enormous computational time if the step size is too small. Secondly, consider step 5 above. When random noise is considered, it is imposssible to know when the point has reached its maximum. The only solution to this problem seems to be scanning through the entire fringe contrast, and calculating the average of the maxima points. However, this defeats our initial purpose of optimizing mirror alignment without scanning the fringe contrast pattern, which is time consuming. More importantly, the fundamental assumption in this algorithm is that the mirror degrees of freedom are completely independent of each other. This is unlikely to be true in the real crackle experiment setup.

5.4 Tackling misalignment (gradient ascent method)

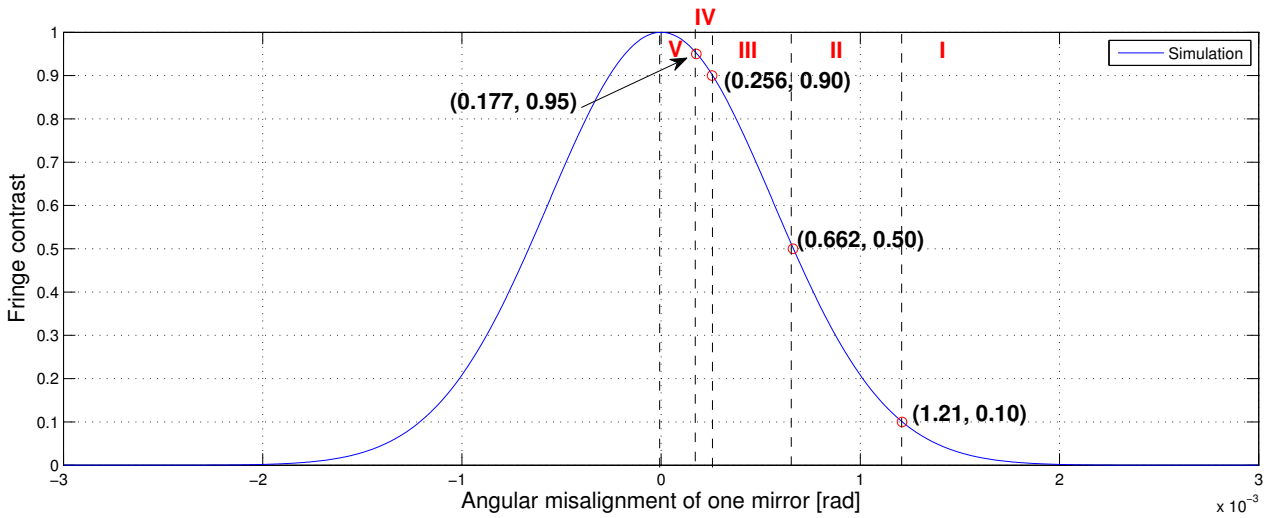

Figure 14: Fringe contrast pattern, divided into 5 different regions. Red points show the upper and lower bound of each region

Owing to various disadvantages of the method above, we adopt an alternative method, called the gradient ascent optimization method [7]. This new approach measures the direction of steepest gradient, i.e. largest change in fringe contrast per unit angular displacement, in the 4-parameter space, and moves the operating point towards the global maximum by iteration. It also allows all four degrees of freedom to be adjusted simultaneously at each iteration, which overcomes the possible angular dependencies between one another, as discussed in the previous subsection.

The crucial parameter in the gradient ascent optimization method is the step size. If the measured fringe contrast is small at a given operating point, we use large step sizes to increase the rate of convergence. This is also important when measurement uncertainty in fringe contrast is considered, which significantly affects fringe contrast measurements at low powers. If the measured fringe contrast is high, we use small step sizes. This can be illustrated by considering Figure 12. Suppose

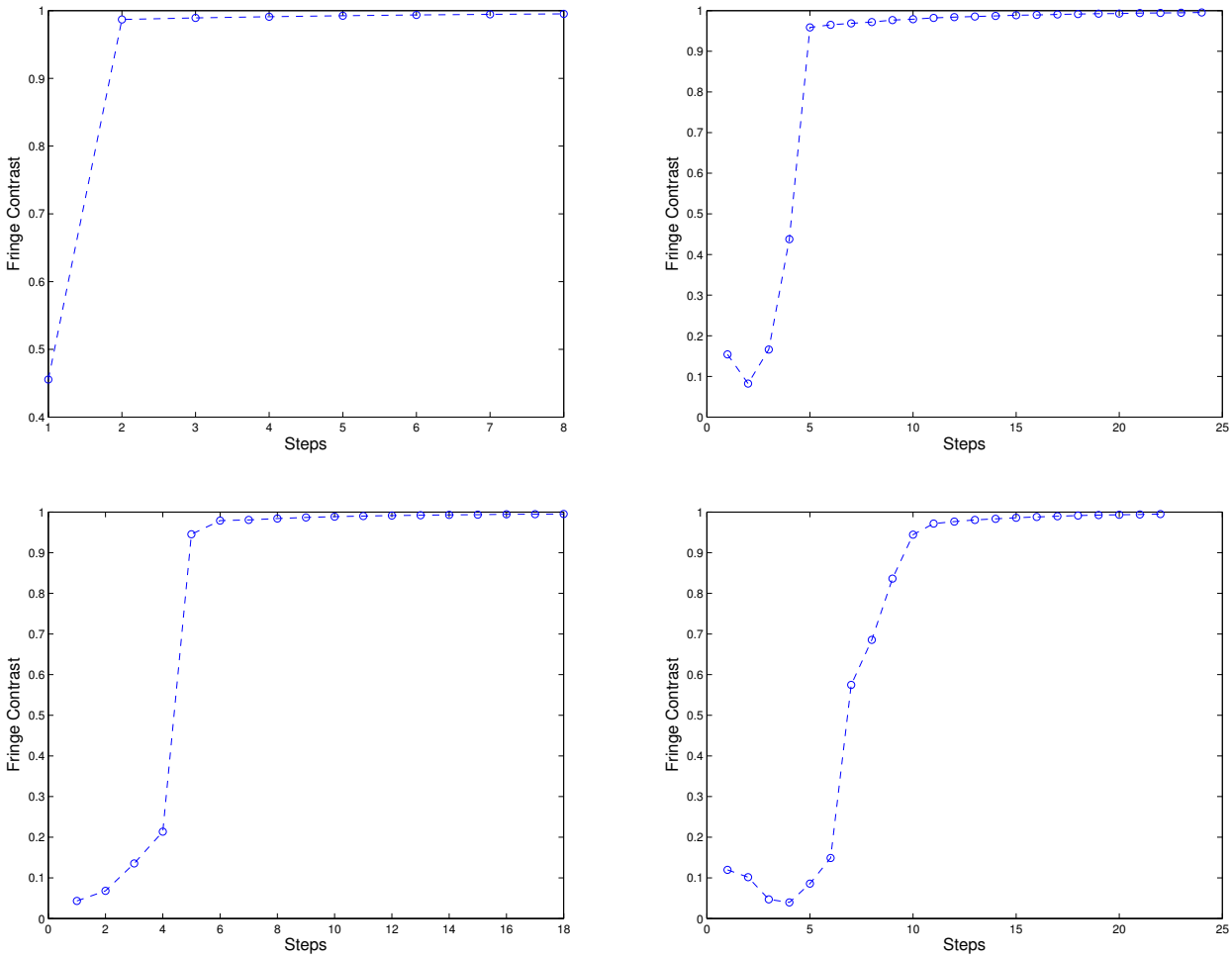

Figure 15: Fringe contrast against number of iterations. Note these figures don't show which degree of freedom is actuated in each step to increase fringe contrast. Refer to figure 16. Oscillations are occasionally observed because random noise is present.

we are at an operating point where fringe contrast is close to unity. If a large step size is used, even though the mirror moves in the correct direction, we 'cross over' the other half of the figure and measures a decrease in fringe contrast.

The conventional adaptive step size method [7] calculates the step size as a function proportional to the local gradient. However, the algorithm only converges linearly, and can be as inefficient as the gradual step method, especially if the operating point has low fringe contrast and local gradient. Here we present slight modification to the conventional approach. Given the fringe contrast pattern in figure 12, we divide the pattern into five regions as shown in Figure 14. We assign a maximum step size, δ_{max} to each region. Recall that in order to avoid 'crossing over' as previously discussed, δ_{max} is the x-value of upper bound point of the region. For example, for region III $\delta_{max} < 0.256 \times 10^{-3}$ rad; for region II $\delta_{max} < 0.662 \times 10^{-3}$ rad. When noise is considered, δ_{max} of each region should be smaller than these values.

In the real experiment, we do not have an expression of the fringe contrast as a function of angular

displacement. Hence, we can only measure the local gradient by perturbing the angular displacement of all degrees of freedom and measure the fringe contrast at the new points. We form a 4 dimensional vector in 4 parameter space, $grad_{local}$, which is the direction of steepest gradient. Then, we calculate the step sizes using the following linear approximation:

$$\delta = \delta_{max} \frac{grad_{local}}{|grad_{max}|} \tag{14}$$

where δ is step size of each degree of freedom, δ_{max} is the maximum step size of each region, $grad_{max}$ is the maximum global gradient of figure 14. By calculating the second order derivative of equation 10, we obtain $grad_{max} = \pm 1075$/rad.

The following steps illustrate our method (see appendix [9, 11]):

1. Measure fringe contrast.
2. Measure the local gradient.
3. Adjust step size, depending on the value of fringe contrast and local gradient as discussed above.
4. Move the mirror along the direction of steepest gradient.
5. Repeat steps 1 to 5 until threshold accuracy is met.

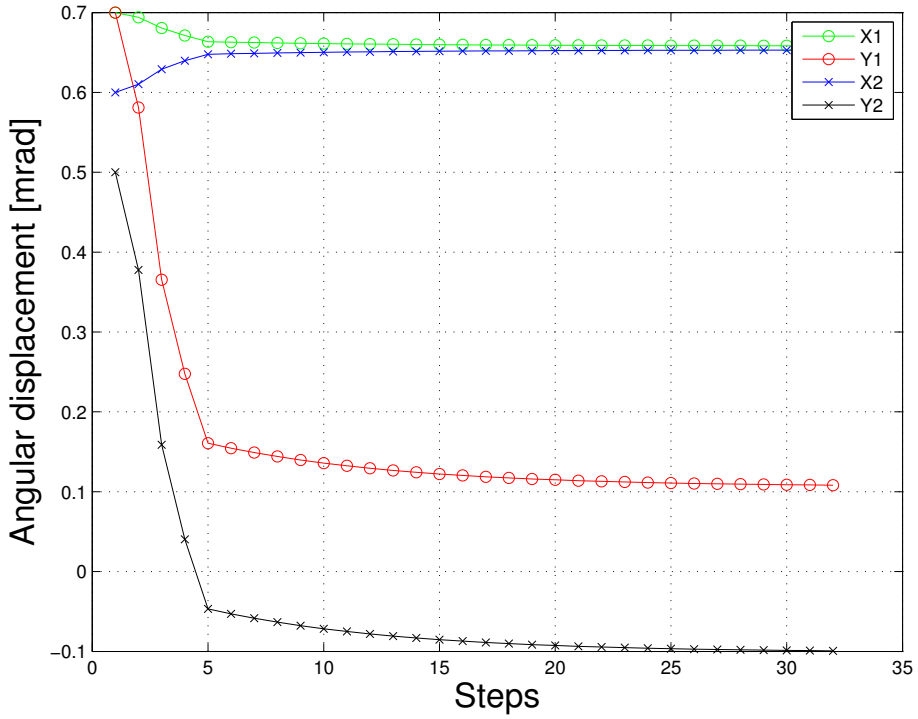

Figure 16: Angular displacement of all degrees of freedom of the bottom-right iteration of figure 15

From figure 15 and 16 this approach to mirror alignment works very well in simulation, and takes up reasonably less time than the first approach. However, one of its limitation is that it might oscillate if the initial operating point is at a low fringe contrast value, like region I in Figure 14.

If the fringe contrast is lower, it might oscillate indefinitely. To avoid this problem, we adopt the gradual step method discussed in the previous section if the operating point falls within region I.

6 Conclusion

The algorithms used to reduce coupling of laser frequency noise, laser intensity noise and the misalignment of Michelson end mirrors have been tested rigorously. The next step is to implement these algorithms in the real crackle experiment.

References

[1] E, Quintero, E. Gustafson, R. Adhikari "Experiment to Investigate Crackle Noise in Maraging Steel Blade Springs" LIGO (2013)

[2] X. Ni, E, Quintero, G. Vajente, "Proposal for an upgrade of the crackle experiment" LIGO (2014)

[3] M. Bassan (editor) Advanced interferometers and the search for gravitational waves, Springer (2014)

[4] G. Vajente, Fast modal simulation of paraxial optical systems: the MIST open source toolbox, Class. Quantum Grav. 30, 075014 (2013)

[5] H. Kogelnik, T. Li, "Laser Beams and Resonators ", Applied Optics, Vol. 5, Issue 10, pp. 1550-1567 (1966)

[6] Siegman, Lasers, University Science Books (1986)

[7] A. Cauchy. Methode generale pour la resolution des syst'emes dequations simultanees. C. R. Acad. Sci. Paris, 25:536538 (1847)

References

[1] Michelson Interferometer Configuration (filename: Crackle_Michelson.mist)

[2] Random Noise (Absoute Uncertainty) (filename: uniform_noise.m)

[3] Random Noise (Percentage Uncertainty) (filename: percentage_noise.m)

[4] Transfer Functions of Mirror Displacement and Laser Frequency Modulations to Output Power at Photodiodes (filename: Crackle_Transfer_Function.m)

[5] Laser Frequency Noise Model vs Simulation (filename: Crackle_Frequency_Noise.m)

[6] Adjust Macroscopic Length Difference to Minimize Laser Frequency Noise Coupling (filename: Crackle_Frequency_Noise_Minimization.m)

[7] Adjust Relative Gain at Symmetric and Antisymmetric Ports (filename: Crackle_Relative_Gain.m)

[8] Fringe Contrast vs Angular Displacement (filename: Crackle_Alignment.m)

[9] Measure Fringe Contrast (filename: f_contrast.m)

[10] Fringe Contrast Optimization by Gradual Step Method (filename: Crackle_Alignment_Gradual_Step.m)

[11] Fringe Contrast Optimization by Gradient Ascent Method (filename: Crackle_Alignment_Gradient_Ascent.m)